Generalized Diffusion Theory for Radiative Transfer in Fully Anisotropic Scattering Media

Original
Generalized Diffusion Theory for Radiative Transfer in Fully Anisotropic Scattering Media / Pini, E., Giusfredi, M., Pattelli, L.. - In: ADVANCED THEORY AND SIMULATIONS. - ISSN 2513-0390. - 9:6(2026). [10.1002/adts.70430]

Publisher:
Wiley-VCH

Published
DOI:10.1002/adts.70430

Advanced Theory and Simulations

ADVANCED THEORY AND SIMULATIONS
www.advtheorysimul.com

RESEARCH ARTICLE OPEN ACCESS

Generalized Diffusion Theory for Radiative Transfer in Fully Anisotropic Scattering Media

Ernesto Pini[1,2] | Michele Giusfredi[3,4,5] | Lorenzo Pattelli[1,2,6]

[1]Istituto Nazionale di Ricerca Metrologica (INRiM), Turin, Italy | [2]European Laboratory for Non-linear Spectroscopy (LENS), Sesto Fiorentino, Italy | [3]Dipartimento di Fisica e Astronomia, Università di Firenze, Sesto Fiorentino, Italy | [4]Istituto dei Sistemi Complessi, Consiglio Nazionale delle Ricerche, Sesto Fiorentino, Italy | [5]Istituto Nazionale di Fisica Nucleare, Sezione di Firenze, Sesto Fiorentino, Italy | [6]Istituto Nazionale di Ottica, Consiglio Nazionale delle Ricerche (CNR-INO), Sesto Fiorentino, Italy

Correspondence: Lorenzo Pattelli (l.pattelli@inrim.it)

Received: 11 February 2026 | **Revised:** 29 April 2026 | **Accepted:** 15 May 2026

Keywords: anisotropic diffusion | monte carlo simulations | photon transport | radiative transfer | scattering media

ABSTRACT

A generalized anisotropic-diffusion framework is developed for transport problems in media described by a tensorial scattering coefficient and a scalar Henyey–Greenstein asymmetry factor. In this regime the classical similarity relation between scattering and transport parameters fails, and each principal diffusion coefficient depends on all components of the microscopic scattering rate. Explicit expressions are derived for the direction-averaged mean free path, the diagonal elements of the diffusion tensor, and boundary condition lengths via rapidly convergent spherical-harmonics expansions, along with open-source implementations. The resulting predictions are validated against anisotropic Monte Carlo simulations, showing excellent agreement across broad ranges of structural anisotropy and phase-function asymmetry factors. The theory provides a compact, general route connecting microscopic anisotropic scattering to macroscopic diffusion coefficients and boundary conditions in bounded geometries.

1 | Introduction

Anisotropic light transport arises whenever the microscopic structure of a material exhibits directional order, leading to different scattering properties along distinct spatial directions and thus an elongated diffuse pattern, as exemplified in Figure 1. Such behavior is observed across a wide range of systems, from biological tissues such as brain white matter [1], spinal cord [2], tendons [3, 4], teeth [5, 6], skin [7] and bone [8], to common materials such as wood [9, 10], paper [11] or compressed foam materials under mechanical deformations [12, 13]. Although anisotropic transport is a common feature in many diffusive media, its quantitative treatment remains elusive. The fundamental difficulty lies in establishing a rigorous link between the microscopic scattering parameters and the macroscopic transport observables in the presence of structural anisotropy. For this reason, even if anisotropic diffusion is detected, it is often disregarded or analyzed using oversimplified models.

An additional level of complexity is introduced when the single scattering phase function, i.e. the angular probability distribution after a scattering event, is also anisotropic. To avoid confusion, this anisotropy is hereby referred to as single scattering "asymmetry". Similarly, the average cosine of the phase function $g = \langle \cos\theta \rangle$, which is sometimes known as the "anisotropy factor", will be referred to as the "asymmetry factor". The phase function

---

Ernesto Pini and Michele Giusfredi contributed equally to this work.

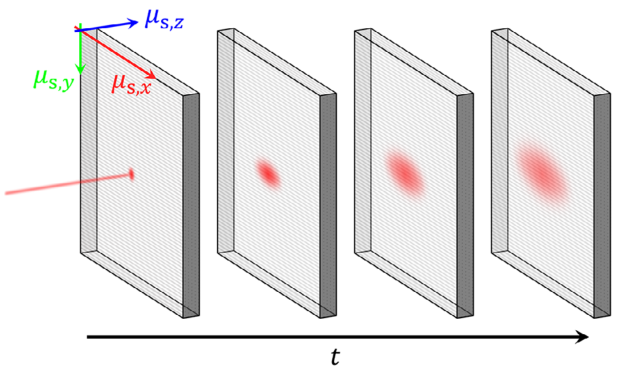

FIGURE 1 | Schematic illustration of the time evolution of the diffuse intensity pattern at the surface of an anisotropic slab following excitation by a point-like pulsed source. Direction-dependent scattering coefficients ($\mu_{\mathrm{s},x}$, $\mu_{\mathrm{s},y}$, $\mu_{\mathrm{s},z}$) lead to anisotropic spreading of light, producing elongated diffusion profiles at increasing time delays. The coordinate system shown defines the reference frame used throughout this work. Adapted from Ref. [11].

depends on the morphology and optical contrast of the scatterers and, for simple geometries such as spheres or cylinders, can be derived analytically from Mie theory. For more complex systems, such as biological tissue, it is commonly approximated by the Henyey–Greenstein function.

In isotropic materials, light transport is well described by the classical diffusion equation, which links the scattering coefficient μ_s to the macroscopic diffusion constant D. In the presence of scattering asymmetry $g \neq 0$, the so-called similarity relation connects the scattering mean free path to its reduced counterpart $\mu_\mathrm{s}' = \mu_\mathrm{s}(1 - g)$, allowing the diffusion coefficient to be expressed in a compact analytic form $D = v/3\mu_\mathrm{s}'$, with v being the speed of light in the medium.

However, in anisotropic media the diffusion process must be described by a tensor that couples the directional diffusion rates $\boldsymbol{D}$ to the underlying scattering properties. A common misconception in this case is represented by treating each diffusion coefficient as depending solely on the scattering coefficient along its corresponding direction, thereby reducing the problem to a naive axis-by-axis extension of the isotropic formalism [4, 14–19].

Several approaches have been proposed to describe anisotropic scattering beyond the diffusion approximation. Among these, Mie theory applied to non-spherical or elongated scatterers provides a direct way to compute both the scattering coefficient and the angular phase function as functions of the incident direction with respect to the principal axis of the scatterer [6, 20–22]. While such microscopic models are physically accurate for highly dilute systems, their application to real materials is often impractical. In some cases, hybrid models have been proposed, based on a mixture of spherical and cylindrical scatterers with different concentrations, dimensions, and optical constants [9, 23, 24]. These assumptions, however, introduce substantial complexity and degrees of freedom, making the inverse retrieval of optical parameters and the prediction of macroscopic observables cumbersome and highly model-dependent.

A more compact and versatile alternative that does not require any assumption on the sample microscopic structure is offered by the tensor-based description of anisotropic transport. In this framework, the directional dependence of the scattering coefficient is represented by a tensor quantity $\boldsymbol{\mu}_\mathrm{s}$, and the diffusion process is formulated as a generalized anisotropic diffusion equation (ADE). This approach captures the essential features of structural anisotropy while retaining the simplicity and robustness of diffusion theory. Importantly, it preserves analytical solvability, enabling closed-form solutions for both time-dependent and steady-state regimes. This possibility has been previously exploited to derive analytical solutions for the special case of uniaxial anisotropy with symmetric scattering, which were validated both numerically and experimentally [13].

In this work, the tensorial diffusion framework is extended to the general case of full anisotropy and non-zero scattering asymmetry. This case is considered specifically (with tensor scattering coefficients and scalar scattering asymmetry) as it represents a significant advancement over the previous description, while being still amenable to a fully analytical description which is likely not feasible when both $\boldsymbol{\mu}_\mathrm{s}$ and $\boldsymbol{g}$ are independent tensors. This generalization preserves the analytical form of the diffusion equation while accounting for more realistic microscopic features of scattering media. Furthermore, the derived solutions include boundary conditions for bounded media (which also exhibit non-trivial dependence on $\boldsymbol{\mu}_\mathrm{s}$ and g), accounting also for Fresnel reflections at the interfaces. These expressions yield complete analytical formulas for evaluating time- and space-resolved transmission and reflection from the semi-infinite and slab geometries, offering a comprehensive framework for modeling light diffusion in structurally anisotropic systems.

2 | From Anisotropic Radiative Transfer to Diffusion Theory

At the microscopic level, structural anisotropy is expressed through a direction-dependent scattering coefficient $\mu_\mathrm{s}(\hat{\mathbf{s}})$, which depends on the unit vector $\hat{\mathbf{s}}$ specifying the propagation direction of an energy packet prior to a scattering event, where $\hat{\mathbf{s}} = (s_x, s_y, s_z) = (\sin\theta\cos\phi,\ \sin\theta\sin\phi,\ \cos\theta)$, with θ and ϕ as the polar and azimuthal angles in the absolute (laboratory) reference frame. In the most general formulation of radiative transfer, other optical properties—including the absorption coefficient, refractive index, and single-scattering phase function—may also depend on direction. While such a fully tensorial description is in principle admissible, it would introduce a large number of independent parameters and severe degeneracies, making both analytical treatment and experimental inference impractical.

The present work therefore focuses on a minimal yet physically expressive setting in which transport anisotropy is entirely encoded in the scattering process. Specifically, the scattering coefficient is allowed to be direction dependent, while absorption, refractive index, and single-scattering asymmetry are treated as scalar parameters. This choice retains the essential consequences of structural anisotropy for macroscopic transport while preserving analytical tractability and a clear connection to experimentally accessible parameters.

Under these assumptions, the extinction coefficient can be written as

$$\mu_{\mathrm{ext}}(\hat{\mathbf{s}}) = \mu_{\mathrm{s}}(\hat{\mathbf{s}}) + \mu_{\mathrm{a}}, \tag{1}$$

with μ_{a} denoting the absorption coefficient. Reciprocity further implies

$$\mu_{\mathrm{ext}}(-\hat{\mathbf{s}}) = \mu_{\mathrm{ext}}(\hat{\mathbf{s}}). \tag{2}$$

Based on these definitions, the Anisotropic Radiative Transfer Equation (ARTE) can be defined analogously to the RTE

$$\begin{aligned}\frac{1}{v}\frac{\partial I(\boldsymbol{r},t,\hat{\mathbf{s}})}{\partial t} &= -\hat{\mathbf{s}}\cdot\boldsymbol{\nabla} I(\boldsymbol{r},t,\hat{\mathbf{s}}) - \mu_{\mathrm{ext}}(\hat{\mathbf{s}}) I(\boldsymbol{r},t,\hat{\mathbf{s}}) \\ &\quad + \int_{4\pi} \mu_{\mathrm{s}}(\hat{\mathbf{s}}')\, I(\boldsymbol{r},t,\hat{\mathbf{s}}')\, p(\hat{\mathbf{s}}',\hat{\mathbf{s}})\mathrm{d}\Omega' + Q(\boldsymbol{r},t,\hat{\mathbf{s}}),\end{aligned} \tag{3}$$

where $I(\boldsymbol{r},t,\hat{\mathbf{s}})$ is the specific intensity, $p(\hat{\mathbf{s}}',\hat{\mathbf{s}})$ the phase function, and $Q(\boldsymbol{r},t,\hat{\mathbf{s}})$ is the source term.

In the diffusive regime, the ARTE leads to a generalized anisotropic diffusion equation (ADE) [25, 26],

$$\left(\frac{\partial}{\partial t} - \boldsymbol{\nabla}\cdot\boldsymbol{D}\boldsymbol{\nabla} + v\mu_{\mathrm{a}}\right)\Phi(\boldsymbol{r},t) = vQ(\boldsymbol{r},t), \tag{4}$$

where $\Phi(\boldsymbol{r},t)$ denotes the fluence rate and $\boldsymbol{D}$ is the anisotropic diffusion tensor,

$$\boldsymbol{D} = \begin{pmatrix} D_{xx} & D_{xy} & D_{xz} \\ D_{yx} & D_{yy} & D_{yz} \\ D_{zx} & D_{zy} & D_{zz} \end{pmatrix}. \tag{5}$$

In the following, it is assumed that the directional dependence of the scattering coefficient can be expressed using nine scalar components of a scattering tensor $\boldsymbol{\mu}_{\mathrm{s}}$,

$$\boldsymbol{\mu}_{\mathrm{s}} = \begin{pmatrix} \mu_{\mathrm{s},xx} & \mu_{\mathrm{s},xy} & \mu_{\mathrm{s},xz} \\ \mu_{\mathrm{s},yx} & \mu_{\mathrm{s},yy} & \mu_{\mathrm{s},yz} \\ \mu_{\mathrm{s},zx} & \mu_{\mathrm{s},zy} & \mu_{\mathrm{s},zz} \end{pmatrix}, \tag{6}$$

such that $\mu_{\mathrm{s}}(\hat{\mathbf{s}}) = \hat{\mathbf{s}}\,\boldsymbol{\mu}_{\mathrm{s}}\,\hat{\mathbf{s}}^{\mathsf{T}}$. While analogous tensorial descriptions could in principle also be introduced for absorption, refractive index, or single-scattering asymmetry, restricting anisotropy to the scattering coefficient alone already captures the dominant impact of structural organization on diffusive transport and yields a framework that remains both analytically tractable and experimentally relevant, since introducing multiple direction-dependent quantities would rapidly lead to an underconstrained and highly degenerate inverse problem.

A general theoretical framework linking microscopic transport statistics to macroscopic diffusion has been developed by Vasques and Larsen [25], encompassing both non-classical propagation regimes and angle-dependent step-length distributions. Within this formulation, anisotropic transport can be described through integral expressions for the diffusion tensor [26]. However, explicit solutions to these expressions have not been reported nor validated against Monte Carlo simulations.

In the first part of the derivation, an isotropic phase function ($g = 0$) is assumed to isolate the effect of direction-dependent scattering on the diffusion process. The extension to the case with $g \neq 0$ is presented in Section 4. Under these assumptions, the diffusion tensor elements can be written as

$$D_{ij} = \frac{v}{4\pi\langle\ell\rangle}\int_{4\pi}\frac{s_i s_j}{\mu_{\mathrm{s}}^2(\hat{\mathbf{s}})}\mathrm{d}\Omega, \tag{7}$$

where $i,j \in \{x,y,z\}$ and $\langle\ell\rangle$ denotes the direction-averaged mean free path. Introducing $\ell(\hat{\mathbf{s}}) = 1/\mu_{\mathrm{s}}(\hat{\mathbf{s}})$ as the direction-dependent scattering mean free path, one has

$$\langle\ell\rangle = \int_{4\pi}\xi(\hat{\mathbf{s}})\ell(\hat{\mathbf{s}})\mathrm{d}\Omega, \tag{8}$$

with $\xi(\hat{\mathbf{s}})$ the probability density for a walker to travel within $\mathrm{d}\Omega$ around direction $\hat{\mathbf{s}}$ after a scattering event. For an isotropic phase function that is independent of the incoming direction, and $\xi(\hat{\mathbf{s}}) = 1/4\pi$.

If a set of principal axes of the microstructure can be identified and aligned with the laboratory Cartesian axes, the scattering tensor $\boldsymbol{\mu}_{\mathrm{s}}$ may be taken as diagonal. In this case, symmetry considerations in Equation (7) imply that the off-diagonal diffusion coefficients vanish, and a more compact single-subscript notation is adopted

$$\boldsymbol{D} = \begin{pmatrix} D_x & 0 & 0 \\ 0 & D_y & 0 \\ 0 & 0 & D_z \end{pmatrix}, \qquad \boldsymbol{\mu}_{\mathrm{s}} = \begin{pmatrix} \mu_{\mathrm{s},x} & 0 & 0 \\ 0 & \mu_{\mathrm{s},y} & 0 \\ 0 & 0 & \mu_{\mathrm{s},z} \end{pmatrix}. \tag{9}$$

In analogy with the isotropic diffusion relation, it is convenient to introduce direction-dependent reduced scattering coefficients $\mu'_{\mathrm{s},i}$ through

$$D_i = \frac{1}{3}\frac{v}{\mu'_{\mathrm{s},i}}, \tag{10}$$

and the associated transport mean free paths $\ell^*_i = 1/\mu'_{\mathrm{s},i}$. It is important to stress that, even for $g = 0$, one generally has $\mu'_{\mathrm{s},i} \neq \mu_{\mathrm{s},i}$: in anisotropic media, no separable similarity relation exists that connects each $\mu_{\mathrm{s},i}$ to an independent "reduced" counterpart. Accordingly, $\mu'_{\mathrm{s},i}$ (and ℓ^*_i) should be regarded as a parametrization of the macroscopic diffusion tensor rather than as microscopic step-length parameters. Neglecting this coupling between diffusion and the full set of scattering coefficients leads to a generally incorrect application of the isotropic formula,

$$D_i^{\mathrm{simplistic}} = \frac{1}{3}\frac{v}{\mu_{\mathrm{s},i}(1-g)} \neq D_i, \tag{11}$$

which can introduce substantial errors in experimental inversion, with deviations that grow with increasing structural anisotropy.

2.1 | Connecting the Microscopic Properties to the Macroscopic Observables

In a previous work [13], analytical solutions limited to the case of uniaxial anisotropy were presented. These solutions are extended here to the fully anisotropic scattering case, where the principal-axis coefficients can take values $\mu_{s,x} \neq \mu_{s,y} \neq \mu_{s,z}$, while the phase function remains isotropic ($g = 0$).

The direction-dependent scattering coefficient can be written as

$$\mu_s(\hat{\mathbf{s}}) = \mu_s(\theta, \phi) = \mu_{s,x} \sin^2\theta \cos^2\phi + \mu_{s,y} \sin^2\theta \sin^2\phi + \mu_{s,z} \cos^2\theta. \tag{12}$$

Using Equation (8) with $\xi(\hat{\mathbf{s}}) = 1/4\pi$ and $\ell(\hat{\mathbf{s}}) = 1/\mu_s(\hat{\mathbf{s}})$, the direction-averaged mean free path can be expressed in integral form as

$$\langle \ell \rangle = \frac{1}{4\pi} \int_0^{2\pi} d\phi \int_0^{\pi} d\theta \frac{\sin\theta}{\mu_s(\theta, \phi)}, \tag{13}$$

which admits the analytical solution

$$\langle \ell \rangle = \frac{F(\phi, m)}{2\sqrt[4]{\mu_{s,x}\mu_{s,y}(\mu_{s,x} - \mu_{s,z})(\mu_{s,y} - \mu_{s,z})}}, \tag{14}$$

where $F(\phi, m)$ is the incomplete elliptic integral of the first kind and

$$\phi = 2 \arctan \sqrt[4]{\frac{(\mu_{s,x} - \mu_{s,z})(\mu_{s,y} - \mu_{s,z})}{\mu_{s,x}\mu_{s,y}}},$$

$$m = \frac{1}{4}\left(2 + \frac{2\mu_{s,x}\mu_{s,y} - \mu_{s,z}\mu_{s,y} - \mu_{s,x}\mu_{s,z}}{\sqrt{\mu_{s,x}\mu_{s,y}(\mu_{s,x} - \mu_{s,z})(\mu_{s,y} - \mu_{s,z})}}\right). \tag{15}$$

The diagonal diffusion coefficients follow from Equation (7) by setting $i = j$:

$$D_x = \frac{v}{4\pi\langle \ell \rangle} \int_{4\pi} \frac{s_x^2}{\mu_s^2(\hat{\mathbf{s}})} d\Omega = \frac{v}{4\pi\langle \ell \rangle} \int_0^{2\pi} d\phi \int_0^{\pi} d\theta \frac{\sin^3\theta \cos^2\phi}{\mu_s^2(\theta, \phi)} \tag{16}$$

$$D_y = \frac{v}{4\pi\langle \ell \rangle} \int_{4\pi} \frac{s_y^2}{\mu_s^2(\hat{\mathbf{s}})} d\Omega = \frac{v}{4\pi\langle \ell \rangle} \int_0^{2\pi} d\phi \int_0^{\pi} d\theta \frac{\sin^3\theta \sin^2\phi}{\mu_s^2(\theta, \phi)} \tag{17}$$

$$D_z = \frac{v}{4\pi\langle \ell \rangle} \int_{4\pi} \frac{s_z^2}{\mu_s^2(\hat{\mathbf{s}})} d\Omega = \frac{v}{4\pi\langle \ell \rangle} \int_0^{2\pi} d\phi \int_0^{\pi} d\theta \frac{\sin\theta \cos^2\theta}{\mu_s^2(\theta, \phi)}. \tag{18}$$

These relations define the diffusion tensor for any set of principal-axis microscopic scattering coefficients.

From Equation (12), one obtains directly

$$\sin^2\theta \cos^2\phi = \frac{\partial}{\partial \mu_{s,x}} \mu_s(\theta, \phi) \tag{19}$$

$$\sin^2\theta \sin^2\phi = \frac{\partial}{\partial \mu_{s,y}} \mu_s(\theta, \phi) \tag{20}$$

$$\cos^2\theta = \frac{\partial}{\partial \mu_{s,z}} \mu_s(\theta, \phi). \tag{21}$$

Using Equation (19) together with the definition of $\langle \ell \rangle$ in Equation (13), the integral expression for D_x simplifies to

$$D_x = \frac{v}{4\pi\langle \ell \rangle} \int_0^{2\pi} d\phi \int_0^{\pi} d\theta \frac{\sin^3\theta \cos^2\phi}{\mu_s^2(\theta, \phi)} = -\frac{v}{\langle \ell \rangle} \frac{\partial}{\partial \mu_{s,x}} \langle \ell \rangle = -v \frac{\partial}{\partial \mu_{s,x}} \ln\langle \ell \rangle. \tag{22}$$

Similarly, Equations (20) and (21) give

$$D_y = -v \frac{\partial}{\partial \mu_{s,y}} \ln\langle \ell \rangle \tag{23}$$

$$D_z = -v \frac{\partial}{\partial \mu_{s,z}} \ln\langle \ell \rangle. \tag{24}$$

Substituting Equation (14) into Equations (22), (23), or (24) yields analytical expressions for the diffusion coefficients. By symmetry under permutations of the principal axes, it is sufficient to report the result for a generic component D_i

$$D_i = \frac{v}{2}\left[\frac{1}{\mu_{s,i}}\left(1 - \frac{\sqrt{\mu_{s,j}\mu_{s,k}}}{\sqrt{(\mu_{s,j} - \mu_{s,i})(\mu_{s,k} - \mu_{s,i})}}\right) + \frac{1}{\langle \ell \rangle}\mathcal{A}_i\right] \tag{25}$$

where (i, j, k) is any permutation of (x, y, z) and

$$\mathcal{A}_i = \frac{1}{(\mu_{s,j} - \mu_{s,i})(\mu_{s,k} - \mu_{s,i}) + \sqrt{\mu_{s,j}\mu_{s,k}(\mu_{s,j} - \mu_{s,i})(\mu_{s,k} - \mu_{s,i})}} + \frac{(\mu_{s,j}\mu_{s,k})^{1/4} E(\phi_i, m_i)}{\mu_{s,i}\left[(\mu_{s,j} - \mu_{s,i})(\mu_{s,k} - \mu_{s,i})\right]^{3/4}}. \tag{26}$$

with $E(\phi_i, m_i)$ denoting the incomplete elliptic integral of the second kind. The arguments ϕ_i and m_i follow from Equation (15) by substituting $(\mu_{s,x}, \mu_{s,y}, \mu_{s,z}) \to (\mu_{s,j}, \mu_{s,k}, \mu_{s,i})$:

$$\phi_i = \phi(\mu_{s,j}, \mu_{s,k}, \mu_{s,i}) \tag{27}$$

$$m_i = m(\mu_{s,j}, \mu_{s,k}, \mu_{s,i}). \tag{28}$$

Equation (25) applies when $\mu_{s,i} \neq \mu_{s,j} \neq \mu_{s,k}$. For parameter combinations where intermediate expressions become complex, the physically meaningful result is given by $D_i = \mathrm{Re}(D_i)$. All expressions derived in this section reduce to the familiar isotropic limit as $\mu_{s,x}, \mu_{s,y}, \mu_{s,z} \to \mu_s$, as expected.

The ratio between the diffusion coefficients obtained from Equation (25) and their simplistic counterparts from Equation (11)

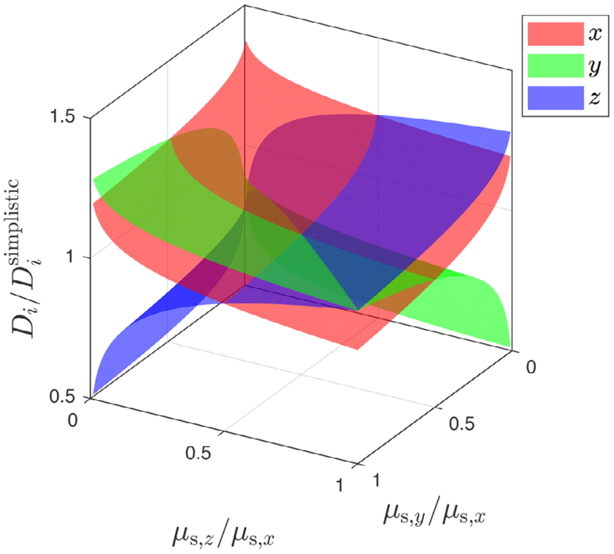

FIGURE 2 | Ratios between the diffusion tensor elements and their corresponding simplistic counterparts for different values of $\mu_{\text{s},y}/\mu_{\text{s},x}$ and $\mu_{\text{s},z}/\mu_{\text{s},x}$, with $\mu_{\text{s},x}$ fixed. This highlights the systematic bias introduced when anisotropy is ignored in diffusion-based parameter estimation.

is reported in Figure 2, while varying $\mu_{\text{s},y}/\mu_{\text{s},x}$ and $\mu_{\text{s},z}/\mu_{\text{s},x}$ in (0,1] at fixed $\mu_{\text{s},x}$. This range encompasses all possible anisotropy ratios because the problem is symmetric under permutation of the principal directions, so ratios larger than 1 can be mapped onto ratios smaller than 1 by exchanging the corresponding axes. The isotropic case corresponds to the central point, where all curves converge to 1. The error introduced by using the simplistic formula Equation (11) increases arbitrarily with anisotropy and can become substantial in regimes relevant, e.g., to common fibrous materials.

3 | ADE Solutions in the Slab Geometry for $g = 0$

In the context of diffusion theory, a commonly studied configuration is that of a slab of thickness L, infinitely extended in the xy plane, illuminated by a pencil beam pulse along the perpendicular z axis, as illustrated in Figure 1. In the diffusive regime, a pencil beam source is more conveniently modeled as an isotropic point source $Q(\boldsymbol{r},t) = \delta(x)\delta(y)\delta(z-z_0)\delta(t)$ placed at the depth z_0 from the surface. Using the method of virtual sources [26], the solution of the time-dependent ADE can be written as:

$$\Phi(\boldsymbol{r},t) = \frac{\mathrm{e}^{-\mu_a v t}\mathrm{e}^{-x^2/(4D_x t)}\mathrm{e}^{-y^2/(4D_y t)}}{(4\pi t)^{3/2}\sqrt{D_x D_y D_z}} \sum_{m=-\infty}^{\infty}\left[\mathrm{e}^{-\frac{(z-z_{+,m})^2}{4D_z t}} - \mathrm{e}^{-\frac{(z-z_{-,m})^2}{4D_z t}}\right] \tag{29}$$

with

$$z_{+,m} = 2m(L+2z_e)+z_0,$$

$$z_{-,m} = 2m(L+2z_e)-2z_e-z_0,$$

representing the position of the virtual sources, and z_e as the extrapolated length.

3.1 | Boundary Conditions

In order to solve the ADE as a function of the microscopic scattering coefficient elements $\mu_{\text{s},i}$, closed-form expressions for z_0 and extrapolated boundary length z_e must be therefore derived.

3.1.1 | Equivalent Isotropic Source Position z_0

The depth position of the equivalent isotropic point-like source z_0 is straightforward when assuming $g = 0$. The depletion of a pencil beam ballistic component entering an anisotropic slab is determined solely by the scattering rate along z, yielding an exponential decay $\mu_{\text{s},z}\exp(-z\mu_{\text{s},z})$, in direct analogy with the isotropic case $\mu_\text{s}\exp(-z\mu_\text{s})$. In this sense, z_0 represents the characteristic distance over which the transport process loses memory of the initial direction $\hat{\mathbf{z}}$. Since for $g = 0$ the phase function is uniform, this memory is lost after a single step, which gives

$$z_0 = \ell_z. \tag{30}$$

3.1.2 | Extrapolated Length z_e

The integral form for the extrapolated length z_e must instead be derived using a general approach that accounts for an anisotropic radiance distribution and Fresnel reflection at the boundaries.

First, let the angular distribution of the radiance in the diffusive limit $P(\hat{\mathbf{s}})$ be defined as the probability density that a random walker is traveling along a direction $\hat{\mathbf{s}}$ after many scattering events. In the most general case, when both the step length and the phase function depend on direction, $P(\hat{\mathbf{s}})$ has a non-trivial dependence on both [27]. For the present case, the diffusive-limit angular distribution depends only on $\boldsymbol{\mu}_\text{s}$ and reads

$$P(\hat{\mathbf{s}}) = \frac{1}{4\pi}\frac{\ell(\hat{\mathbf{s}})}{\langle \ell \rangle} = \frac{1}{4\pi}\frac{1}{\langle \ell \rangle \mu_\text{s}(\hat{\mathbf{s}})}. \tag{31}$$

Notably, although Equation (31) is introduced here for $g = 0$, it also holds for $g \neq 0$ under the present assumptions, because the phase function remains independent of the incoming direction. Figure 3 shows examples of $P(\hat{\mathbf{s}})$ for different illustrative configurations of structural anisotropy.

For a refractive index contrast $n = n_\text{in}/n_\text{ext}$ between the medium and the external environment, the polarization-averaged Fresnel reflectance for incident angle θ is

$$R(\theta) = \frac{1}{2}\left[\left(\frac{n\cos\theta - \sqrt{1-n^2\sin^2\theta}}{n\cos\theta + \sqrt{1-n^2\sin^2\theta}}\right)^2 + \left(\frac{n\sqrt{1-n^2\sin^2\theta} - \cos\theta}{n\sqrt{1-n^2\sin^2\theta} + \cos\theta}\right)^2\right]. \tag{32}$$

Following the notation of Alerstam [27], the extrapolated length can be expressed as

$$z_e = \frac{\mathcal{C}+\mathcal{Y}}{\mathcal{B}-\mathcal{X}}, \tag{33}$$

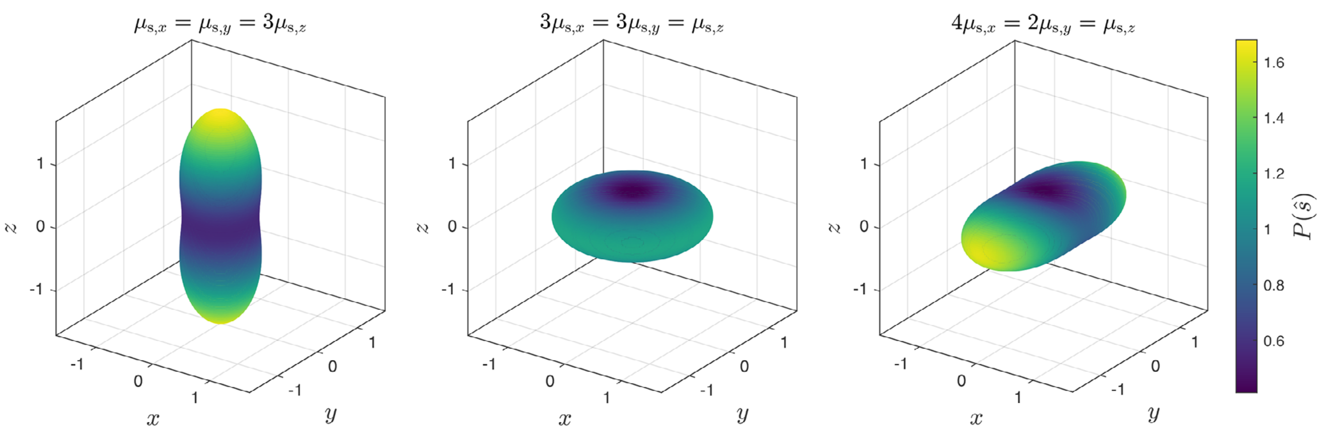

FIGURE 3 | Representation of the angular distribution of the radiance $P(\hat{\mathbf{s}})$ in the diffusive limit for different anisotropic scattering configurations.

where

$$\mathcal{B} = \int_{\Omega_{\text{up}}} P(\hat{\mathbf{s}}) s_z \mathrm{d}\Omega = \frac{1}{4\pi\langle \ell \rangle} \int_0^{\pi/2} \mathrm{d}\theta \int_0^{2\pi} \mathrm{d}\phi \frac{\sin\theta\cos\theta}{\mu_{\text{s}}(\theta,\phi)}, \quad (34)$$

$$\mathcal{C} = \int_{\Omega_{\text{up}}} P(\hat{\mathbf{s}}) \ell(\hat{\mathbf{s}}) s_z^2 \mathrm{d}\Omega = \frac{1}{4\pi\langle \ell \rangle} \int_0^{\pi/2} \mathrm{d}\theta \int_0^{2\pi} \mathrm{d}\phi \frac{\sin\theta\cos^2\theta}{\mu_{\text{s}}^2(\theta,\phi)}, \quad (35)$$

$$\mathcal{X} = \int_{\Omega_{\text{up}}} P(\hat{\mathbf{s}}) s_z R(\theta) \mathrm{d}\Omega = \frac{1}{4\pi\langle \ell \rangle} \int_0^{\pi/2} \mathrm{d}\theta \int_0^{2\pi} \mathrm{d}\phi \frac{\sin\theta\cos\theta R(\theta)}{\mu_{\text{s}}(\theta,\phi)}, \quad (36)$$

$$\mathcal{Y} = \int_{\Omega_{\text{up}}} P(\hat{\mathbf{s}}) \ell(\hat{\mathbf{s}}) s_z^2 R(\theta) \mathrm{d}\Omega = \frac{1}{4\pi\langle \ell \rangle} \int_0^{\pi/2} \mathrm{d}\theta \int_0^{2\pi} \mathrm{d}\phi \frac{\sin\theta\cos^2\theta R(\theta)}{\mu_{\text{s}}^2(\theta,\phi)}, \quad (37)$$

where $\Omega_{\text{up}} = 2\pi$ denotes the solid angle of the upper hemisphere.

The analytical solution for $\mathcal{B}$ can be written as

$$\mathcal{B} = -\frac{1}{4\pi\langle \ell \rangle} \frac{\operatorname{arccoth}\left[\frac{2\sqrt{\mu_{s,x}-\mu_{s,z}}\sqrt{\mu_{s,y}-\mu_{s,z}}}{\mu_{s,x}+\mu_{s,y}-2\mu_{s,z}}\right] + \operatorname{arccoth}\left[\frac{2\sqrt{\mu_{s,x}\mu_{s,y}(\mu_{s,x}-\mu_{s,z})}\sqrt{\mu_{s,y}-\mu_{s,z}}}{-2\mu_{s,x}\mu_{s,y}+(\mu_{s,x}+\mu_{s,y})\mu_{s,z}}\right]}{4\sqrt{\mu_{s,x}-\mu_{s,z}}\sqrt{\mu_{s,y}-\mu_{s,z}}}. \quad (38)$$

For $\mathcal{C}$ it can be shown that

$$\mathcal{C} = \frac{D_z}{2v}. \quad (39)$$

The integrals $\mathcal{X}$ and $\mathcal{Y}$, on the other hand, must be typically evaluated numerically, while they vanish for a matched refractive index ($n = 1$).

Equivalently, the extrapolated length can be expressed in the unified integral form

$$z_{\text{e}} = \frac{\int_0^{\pi/2} \mathrm{d}\theta \int_0^{2\pi} \mathrm{d}\phi \frac{\sin\theta\cos^2\theta}{\mu_{\text{s}}^2(\theta,\phi)} [1 + R(\theta)]}{\int_0^{\pi/2} \mathrm{d}\theta \int_0^{2\pi} \mathrm{d}\phi \frac{\sin\theta\cos\theta}{\mu_{\text{s}}(\theta,\phi)} [1 - R(\theta)]}. \quad (40)$$

4 | ADE Solutions in the Slab Geometry for $g \neq 0$

The anisotropic diffusion framework is now extended to include the effect of a scalar single-scattering asymmetry factor g. Although in structurally anisotropic systems the phase function may itself depend on direction, leading to a 3 × 3 tensor asymmetry factor [27], here the description is deliberately restricted to the scalar range $-1 < g < 1$. This choice avoids cross-talk between multiple tensorial quantities, which would generally prevent the unique determination of optical parameters, reflects the absence of a consolidated framework for direction-dependent asymmetry factors in the literature, and simplifies the problem by preserving the azimuthal symmetry of the phase function.

A widely adopted model for single scattering in complex media is the Henyey–Greenstein phase function,

$$p(\cos\theta) = \frac{1 - g^2}{4\pi(1 + g^2 - 2g\cos\theta)^{3/2}}, \quad (41)$$

which has proven effective in describing multiple scattering in many realistic systems, including biological tissues [26].

Because the phase function remains independent of the incoming direction prior to scattering, the direction-averaged mean free path $\langle \ell \rangle$ retains the same form as in the $g = 0$ case (Equation (14)). For the same reason, the angular distribution of the radiance $P(\hat{\mathbf{s}})$ remains unchanged (Equation (31)). Conversely, the diffusion

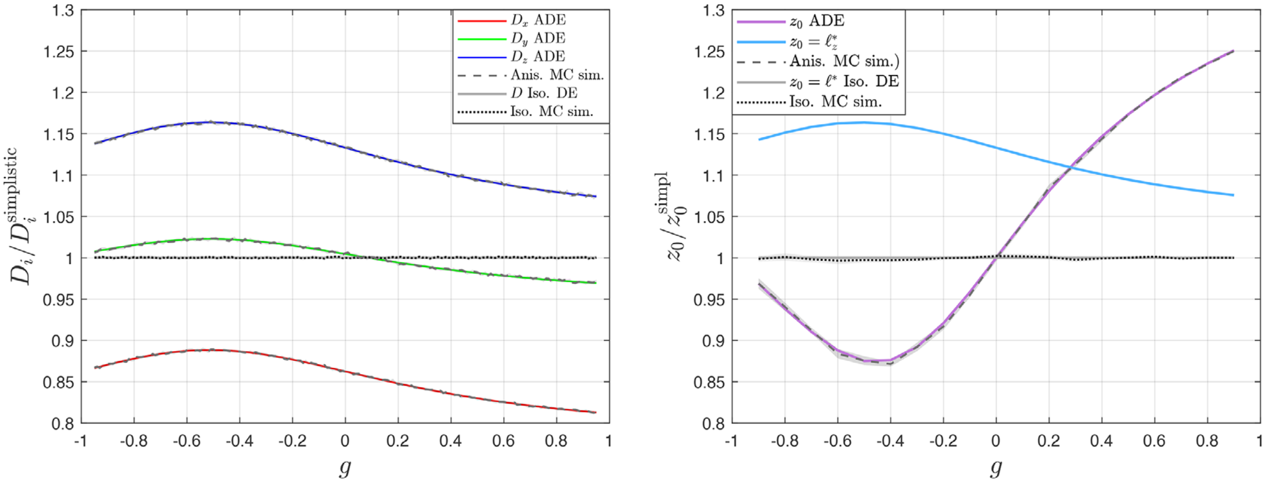

FIGURE 4 | (a) Ratios between the diffusion tensor elements and their corresponding simplistic approximations as a function of the asymmetry factor g. Solid colored curves denote the analytical predictions, while black dashed curves show anisotropic Monte Carlo results. Shaded areas indicate 2σ confidence intervals. Results are shown for $4\mu_{s,x} = 2\mu_{s,y} = \mu_{s,z}$, no free parameters are used in the analytical curves. The gray curve represents the isotropic case. (b) Corresponding ratios for the equivalent isotropic source position z_0. The light blue curve representing the previously proposed approximation [27] $z_0 = \ell_z^*$ is shown for comparison.

tensor must be re-derived, because scattering asymmetry introduces persistent angular correlations that affect the macroscopic transport rates. The full derivation is presented in Appendix A; here only the final result for a generic diagonal diffusion tensor element D_i, expressed as an infinite expansion over spherical harmonics $Y_l^m(\hat{\mathbf{s}})$, is reported

$$D_i = D_i\Big|_{g=0} + \frac{v}{4\pi\langle\ell\rangle}\sum_{n=0}^{\infty}\frac{g^{2n+1}}{1-g^{2n+1}}\sum_{m=-n}^{n}\left|H^i_{2n+1,2m}\right|^2, \tag{42}$$

where

$$H^i_{lm} = \int_{4\pi}\frac{s'_i Y_l^m(\hat{\mathbf{s}}')}{\mu_s(\hat{\mathbf{s}}')}\mathrm{d}\Omega'. \tag{43}$$

These expressions were validated against Monte Carlo simulations of random walkers propagating in an infinite anisotropic scattering medium over a wide range of asymmetry factors g. Figure 4a shows the ratio between the diffusion tensor elements and the commonly used simplistic expressions. For the illustrative anisotropic configuration $4\mu_{s,x} = 2\mu_{s,y} = \mu_{s,z}$, at least one diffusion coefficient deviates by more than 10 % across the entire range of $-1 < g < 1$. By contrast, in the isotropic limit $\mu_s(\hat{\mathbf{s}}) = \mu_s$, the similarity relation remains exact for all values of g, in full agreement with Monte Carlo results. In this case, Equation (42) correctly reduces to the standard expression $D = v/[3\mu_s(1-g)]$.

4.1 | Boundary Conditions

When scattering asymmetry is present, both the equivalent isotropic source depth z_0 and the extrapolated length z_e acquire a non-trivial dependence on g and on the full scattering tensor. For $g \neq 0$, the microscopic mean free path $\ell(\hat{\mathbf{s}})$ entering the boundary-condition integrals $\mathcal{B}$, $\mathcal{C}$, $\mathcal{X}$ and $\mathcal{Y}$ (Equations (34)–(37)) no longer represents the correct length scale. A previously proposed approximation to overcome the simplistic approach replaces $\ell(\hat{\mathbf{s}})$ with the transport length $\ell^*(\hat{\mathbf{s}})$ inferred from the diffusion tensor and assumes $z_0 = \ell_z^*$ [27]. However, this approach neglects the finite angular persistence induced by the phase function and becomes increasingly inaccurate for small g and strong anisotropy.

4.1.1 | Equivalent Isotropic Source Position z_0

For $g \neq 0$, the source depth z_0 is linked to the cumulative directional memory of the random walk rather than its asymptotic diffusion rate. A new length scale must therefore be evaluated explicitly from the underlying scattering kernel. To this end, a *direction-dependent persistence length* $\lambda(\hat{\mathbf{s}})$ is introduced, representing the characteristic distance over which the transport process loses memory of the initial direction $\hat{\mathbf{s}}$. The full derivation is given in Appendix B. For a Henyey–Greenstein phase function, $\lambda(\hat{\mathbf{s}})$ can be written as

$$\lambda(\hat{\mathbf{s}}) = \sum_{n=0}^{\infty}\frac{4n+3}{4\pi}\frac{1}{1-g^{2n+1}}\int_{4\pi}\frac{\hat{\mathbf{s}}\cdot\hat{\mathbf{s}}' P_{2n+1}(\hat{\mathbf{s}}\cdot\hat{\mathbf{s}}')}{\mu_s(\hat{\mathbf{s}}')}\mathrm{d}\Omega', \tag{44}$$

where P_{2n+1} denotes the Legendre polynomial of order $2n+1$. The equivalent isotropic source depth then generalizes to

$$z_0 = \lambda_z = \lambda(\hat{\mathbf{z}}). \tag{45}$$

The accuracy of Equation (45) was assessed by Monte Carlo simulations in which random walkers are initialized with a pencil-beam angular distribution along $\hat{\mathbf{z}}$ and propagated in an infinite anisotropic scattering medium. After a sufficiently large number of scattering events, the ensemble-averaged displacement along z converges to z_0. Results are shown in Figure 4b as a ratio with respect to the commonly used approximation $z_0^{\text{simplistic}} = \ell_z/(1-g)$.

4.1.2 | Extrapolated Length z_e

The extrapolated length z_e depends on the asymptotic diffusion rate along z and on the refractive index contrast n. Since the stationary radiance distribution $P(\hat{\mathbf{s}})$ remains independent of g under the present assumptions, the boundary integrals $\mathcal{B}$ and $\mathcal{X}$ are unchanged. The integral C is directly linked to D_z via Equation (39), and therefore the diffusion rate along z must be evaluated using Equation (42). The Fresnel-weighted term $\mathcal{Y}$ accounts for boundary reflections, and its general expression becomes

$$\mathcal{Y} = \mathcal{Y}\Big|_{g=0} + \frac{1}{4\pi\langle\ell\rangle}\sum_{n=0}^{\infty}\frac{g^{2n+1}}{1-g^{2n+1}}\sum_{m=-n}^{n} H^z_{2n+1,m}\widetilde{H}^z_{2n+1,m}, \tag{46}$$

where $H^z_{2n+1,m}$ denotes the z component of Equation (43), and

$$\widetilde{H}^z_{2n+1,m} = \int_{\Omega_{\mathrm{up}}} \frac{s_z}{\mu_{\mathrm{s}}(\hat{\mathbf{s}})} Y^*_{2n+1,m}(\hat{\mathbf{s}}) R(\theta)\,\mathrm{d}\Omega \tag{47}$$

with $R(\theta)$ as the Fresnel reflectance defined in Equation (32). The term $\mathcal{Y}\Big|_{g=0}$ corresponds to the isotropic-scattering contribution and includes the same Fresnel weighting over the upper hemisphere. A detailed derivation of Equation (46), including the hemisphere-restricted angular projections and the inclusion of Fresnel reflections, is provided in Appendix C. Finally, the extrapolated length is evaluated using Equation (33).

5 | Time- and Space-Dependent Solutions of ADE

The results presented in the previous section are validated using the open source Monte Carlo package PyXOpto [28], which has been modified to handle anisotropic scattering and asymmetry factors. The ADE solutions presented here in the time and space domains are also made available as a set of Python and MATLAB functions at https://github.com/epini/ADE , where the integrals to evaluate the macroscopic transport properties are solved numerically.

Time-resolved reflected and transmitted intensity profiles for a slab illuminated along the z axis can be obtained from the fluence rate in Equation (29) using Fick's law [26, 29] by setting

$$R(x,y,t) = \frac{D_z}{v}\frac{\partial}{\partial z}\Phi(x,y,z=0,t), \tag{48}$$

$$T(x,y,t) = -\frac{D_z}{v}\frac{\partial}{\partial z}\Phi(x,y,z=L,t), \tag{49}$$

resulting in bi-variate Gaussian distributions:

$$\begin{aligned}R(x,y,t) = &-\frac{v\exp(-\mu_{\mathrm{a}}vt)\exp\left(-\frac{x^2}{4D_xt}\right)\exp\left(-\frac{y^2}{4D_yt}\right)}{2(4\pi)^{3/2}t^{5/2}\sqrt{D_xD_yD_z}}\\ &\times\sum_{m=-\infty}^{\infty}\left[z_{3,m}\exp\left(-\frac{z_{3,m}^2}{4D_zt}\right)-z_{4,m}\exp\left(-\frac{z_{4,m}^2}{4D_zt}\right)\right],\end{aligned} \tag{50}$$

$$\begin{aligned}T(x,y,t) = &\frac{v\exp(-\mu_{\mathrm{a}}vt)\exp\left(-\frac{x^2}{4D_xt}\right)\exp\left(-\frac{y^2}{4D_yt}\right)}{2(4\pi)^{3/2}t^{5/2}\sqrt{D_xD_yD_z}}\times\\ &\times\sum_{m=-\infty}^{\infty}\left[z_{1,m}\exp\left(-\frac{z_{1,m}^2}{4D_zt}\right)-z_{2,m}\exp\left(-\frac{z_{2,m}^2}{4D_zt}\right)\right],\end{aligned} \tag{51}$$

where

$$\begin{aligned}z_{1,m} &= L(1-2m)-4mz_{\mathrm{e}}-z_0,\\ z_{2,m} &= L(1-2m)-(4m-2)z_{\mathrm{e}}+z_0,\\ z_{3,m} &= -2mL-4mz_{\mathrm{e}}-z_0,\\ z_{4,m} &= -2mL-(4m-2)z_{\mathrm{e}}+z_0.\end{aligned}$$

The Mean Square Displacements (MSD) along x and y are

$$w_x^2(t) = 4D_xt, \qquad w_y^2(t) = 4D_yt. \tag{52}$$

Accessing either $R(x,y,t)$ or $T(x,y,t)$ at different times enables the direct retrieval of the diffusion rates along x and y. Moreover, the evolution of $w_x^2(t)$ and $w_y^2(t)$ does not depend on the amplitude of the profile, so that any effect that may modify its overall intensity, such as a homogeneous absorption coefficient, factors out exactly from the MSD.

Total time-resolved reflectance and transmittance expressions can be derived by direct integration of Equations (50) and (51) in space

$$\begin{aligned}R(t) = &-\frac{\exp(-\mu_{\mathrm{a}}vt)}{2(4\pi D_z)^{1/2}t^{3/2}}\sum_{m=-\infty}^{\infty}\\ &\times\left[z_{3,m}\exp\left(-\frac{z_{3,m}^2}{4D_zt}\right)-z_{4,m}\exp\left(-\frac{z_{4,m}^2}{4D_zt}\right)\right],\end{aligned} \tag{53}$$

$$\begin{aligned}T(t) = &\frac{\exp(-\mu_{\mathrm{a}}vt)}{2(4\pi D_z)^{1/2}t^{3/2}}\sum_{m=-\infty}^{\infty}\\ &\times\left[z_{1,m}\exp\left(-\frac{z_{1,m}^2}{4D_zt}\right)-z_{2,m}\exp\left(-\frac{z_{2,m}^2}{4D_zt}\right)\right].\end{aligned} \tag{54}$$

The steady state profiles are obtained integrating Equations (50) and (51) in time

$$\begin{aligned}R(x,y) = &-\frac{1}{4\pi\sqrt{D_xD_yD_z}}\sum_{m=-\infty}^{\infty}\Bigg[z_{3,m}\left(\frac{x^2}{D_x}+\frac{y^2}{D_y}+\frac{z_{3,m}^2}{D_z}\right)^{-3/2}\\ &\times\left(1+\sqrt{\mu_{\mathrm{a}}v\left(\frac{x^2}{D_x}+\frac{y^2}{D_y}+\frac{z_{3,m}^2}{D_z}\right)}\right)\\ &\times\exp\left(-\sqrt{\mu_{\mathrm{a}}v\left(\frac{x^2}{D_x}+\frac{y^2}{D_y}+\frac{z_{3,m}^2}{D_z}\right)}\right)\\ &-z_{4,m}\left(\frac{x^2}{D_x}+\frac{y^2}{D_y}+\frac{z_{4,m}^2}{D_z}\right)^{-3/2}\\ &\times\left(1+\sqrt{\mu_{\mathrm{a}}v\left(\frac{x^2}{D_x}+\frac{y^2}{D_y}+\frac{z_{4,m}^2}{D_z}\right)}\right)\\ &\times\exp\left(-\sqrt{\mu_{\mathrm{a}}v\left(\frac{x^2}{D_x}+\frac{y^2}{D_y}+\frac{z_{4,m}^2}{D_z}\right)}\right)\Bigg],\end{aligned} \tag{55}$$

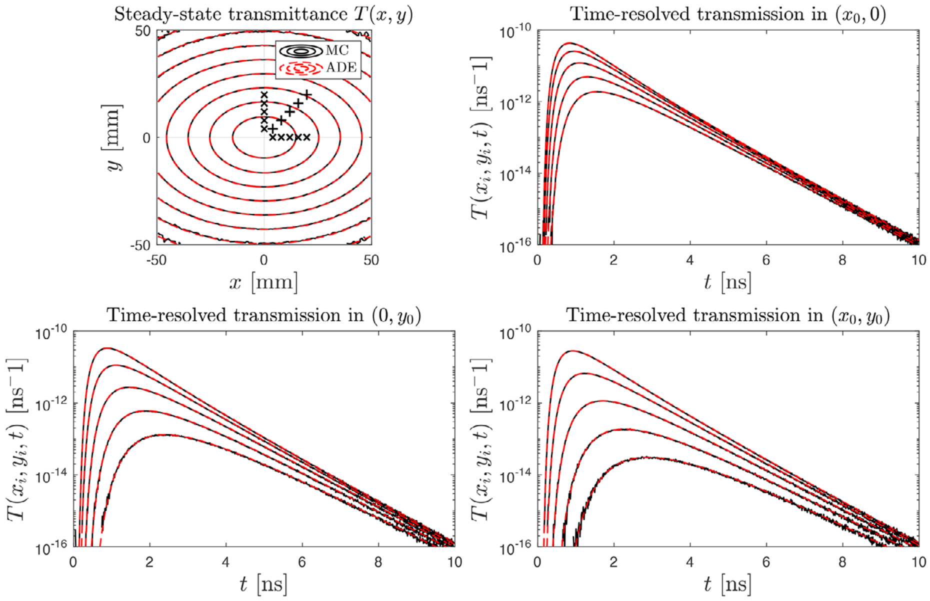

FIGURE 5 | (a) Steady-state transmittance $T(x,y)$ from a 10 mm-thick slab with $\mu_{s,x} = 2.5\ \mathrm{mm}^{-1}$, $\mu_{s,y} = 7.5\ \mathrm{mm}^{-1}$, $\mu_{s,z} = 10\ \mathrm{mm}^{-1}$, $n = 1.3$, $\mu_a = 2 \times 10^{-6}\ \mathrm{mm}^{-1}$, and $g = 0$. Data are plotted as log-scale contour lines marking consecutive decades. (b–d) Time-resolved transmittance at different locations (x_0, y_0) on the slab's output surface, identified by the markers in panel (a). The prediction from anisotropic theory (dashed) is compared against the results of a Monte Carlo simulation with 10^{12} trajectories.

$$
\begin{aligned}
T(x,y) = \frac{1}{4\pi\sqrt{D_xD_yD_z}} \sum_{m=-\infty}^{\infty} \Bigg[& z_{1,m}\left(\frac{x^2}{D_x}+\frac{y^2}{D_y}+\frac{z_{1,m}^2}{D_z}\right)^{-3/2} \\
& \times\left(1+\sqrt{\mu_a v\left(\frac{x^2}{D_x}+\frac{y^2}{D_y}+\frac{z_{1,m}^2}{D_z}\right)}\right) \\
& \times\exp\left(-\sqrt{\mu_a v\left(\frac{x^2}{D_x}+\frac{y^2}{D_y}+\frac{z_{1,m}^2}{D_z}\right)}\right) \\
& -z_{2,m}\left(\frac{x^2}{D_x}+\frac{y^2}{D_y}+\frac{z_{2,m}^2}{D_z}\right)^{-3/2} \\
& \times\left(1+\sqrt{\mu_a v\left(\frac{x^2}{D_x}+\frac{y^2}{D_y}+\frac{z_{2,m}^2}{D_z}\right)}\right) \\
& \times\exp\left(-\sqrt{\mu_a v\left(\frac{x^2}{D_x}+\frac{y^2}{D_y}+\frac{z_{2,m}^2}{D_z}\right)}\right)\Bigg]. \qquad (56)
\end{aligned}
$$

Finally, integrating in time Equations (53) and (54) gives the total reflectance and transmittance

$$
\begin{aligned}
R = -\frac{1}{2}\sum_{m=-\infty}^{\infty} \Bigg[& \mathrm{sgn}(z_{3,m})\exp\left(-|z_{3,m}|\sqrt{\frac{\mu_a v}{D_z}}\right) \\
& -\mathrm{sgn}(z_{4,m})\exp\left(-|z_{4,m}|\sqrt{\frac{\mu_a v}{D_z}}\right)\Bigg], \qquad (57)
\end{aligned}
$$

$$
\begin{aligned}
T = \frac{1}{2}\sum_{m=-\infty}^{\infty} \Bigg[& \mathrm{sgn}(z_{1,m})\exp\left(-|z_{1,m}|\sqrt{\frac{\mu_a v}{D_z}}\right) \\
& -\mathrm{sgn}(z_{2,m})\exp\left(-|z_{2,m}|\sqrt{\frac{\mu_a v}{D_z}}\right)\Bigg]. \qquad (58)
\end{aligned}
$$

Equations (57) and (58) can be used only for $\mu_a > 0$, thus the total absorbance can be evaluated as $A = 1 - R - T$. In the case of a non-absorbing optically thick slab ($L \gg \langle \ell \rangle$) the usual scaling of the total transmittance with thickness holds as

$$
T = \frac{z_0 + z_e}{L + 2z_e}. \qquad (59)
$$

Equation (59) is analogous to the isotropic formula for total transmission [26], where the presence of anisotropy is now taken into account in z_e and z_0. Therefore, the total reflectance can be retrieved as $R = 1 - T$.

To validate these solutions, a set of MC simulations was performed for the time- and space-resolved transmittance $T(x,y,t)$ for anisotropic slabs with various optical properties. Results are reported for two representative cases with full anisotropy, mismatched refractive index contrast, non-zero absorption, and $g = \{0, 0.9\}$. The Monte Carlo outputs are compared to the numerically evaluated ADE predictions (Figures 5 and 6), showing excellent agreement in both cases.

6 | Discussion

In this work, a generalized diffusion framework for light transport in fully anisotropic scattering media has been developed. By explicitly linking a tensorial description of the microscopic scattering coefficient to macroscopic diffusion rates, it has been shown that anisotropic transport cannot be described by a simplistic extension of the classical isotropic diffusion independently along each axis. A central result is that each diagonal element of the diffusion tensor depends on all components of the scattering tensor. This coupling becomes increasingly relevant with growing anisotropy and can lead to substantial errors when simplistic

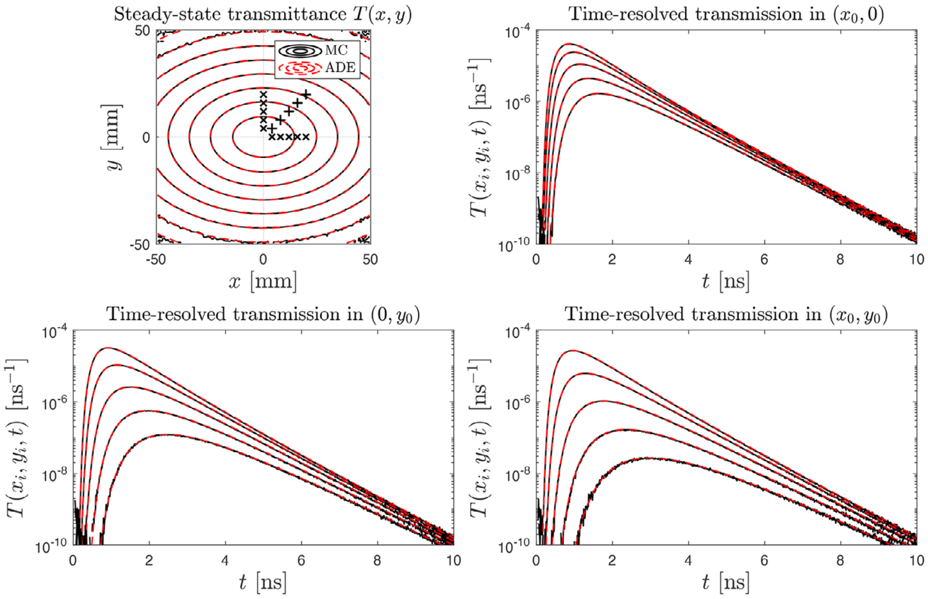

FIGURE 6 | (a) Steady-state transmittance $T(x, y)$ from a 10 mm-thick slab with $\mu_{s,x} = 25\ \text{mm}^{-1}$, $\mu_{s,y} = 75\ \text{mm}^{-1}$, $\mu_{s,z} = 100\ \text{mm}^{-1}$, $n = 1.3$, $\mu_a = 2 \times 10^{-6}\ \text{mm}^{-1}$, and $g = 0.9$. Data are plotted as log-scale contour lines marking consecutive decades. (b–d) Time-resolved transmittance at different locations (x_0, y_0) on the slab's output surface, identified by the markers in panel (a). The prediction from anisotropic theory (dashed) is compared against the results of a Monte Carlo simulation with 10^{12} trajectories.

substitutions are used. The analytical relations derived here, validated against anisotropic Monte Carlo simulations, provide a compact and rigorous framework that retains the form and robustness of diffusion-based modeling.

The inclusion of a scalar single-scattering asymmetry factor extends the model to realistic systems while preserving analytical tractability. Although closed-form expressions are not available for $g \neq 0$, the corresponding analytical series converges rapidly and yields diffusion coefficients in excellent agreement with numerical simulations across the full range of scattering asymmetry $-1 < g < 1$.

Additionally, it is shown that in bounded anisotropic systems, z_0 and z_e depend explicitly on microscopic scattering properties rather than solely on transport mean free paths, highlighting the inapplicability of boundary conditions inherited from isotropic theory. In the presence of scattering asymmetry, z_0 is controlled by a direction-dependent persistence length that quantifies the cumulative angular memory of the random walk, whereas z_e is governed by the asymptotic diffusion rate along the boundary normal together with the refractive index contrast. These results provide a physically consistent interpretation of anisotropic boundary conditions and enable diffusion solutions that accurately reproduce Monte Carlo predictions for time- and space-resolved reflectance and transmittance. From an experimental perspective, these closed-form slab solutions offer a direct route to retrieving anisotropic transport parameters from measured data.

Finally, although the present framework is formulated for radiative transport, its structure is not specific to optics. Closely related transport and diffusion equations arise in the propagation of neutrons and other ionizing particles [25], as well as in diffusive heat transport in anisotropic media [30, 31], where direction-dependent cross sections or mean free paths give rise to tensorial diffusion coefficients. In this broader context, the analytical relations derived here may help connect microscopic transport properties to macroscopic diffusion behavior beyond commonly adopted approximations.

Acknowledgments

The authors thank Fabrizio Martelli, André Liemert and Alwin Kienle for fruitful discussion. This work was partially funded by the European Union's NextGenerationEU Programme with the I-PHOQS Research Infrastructure (IR0000016, ID D2B8D520, CUP B53C22001750006) "Integrated infrastructure initiative in Photonic and Quantum Sciences". L.P. acknowledges the CINECA award under the ISCRA initiative, for the availability of high performance computing resources and support (ISCRA-C "ARTTESC2").

Open access publishing facilitated by Istituto Nazionale di Ricerca Metrologica, as part of the Wiley - CRUI-CARE agreement.

Conflicts of Interest

The authors declare no conflicts of interest.

Data Availability Statement

The scripts and functions that support the findings of this study are openly available on https://github.com/epini/ADE. Anisotropic Monte Carlo simulations have been performed using an open-source software tool https://github.com/xopto/pyxopto.

References

1. E. Pini, D. Di Meo, I. Costantini, et al., "Anisotropic Light Propagation in Human Brain White Matter," *Neurophotonics* 12, no. 4 (2025): 045003, https://doi.org/10.1117/1.NPh.12.4.045003.

2. D. DePaoli, A. Gasecka, M. Bahdine, et al., "Anisotropic Light Scattering from Myelinated Axons in the Spinal Cord," *Neurophotonics* 7, no. 1 (2020): 015011, https://doi.org/10.1117/1.NPh.7.1.015011.

3. E. Simon, P. Krauter, and A. Kienle, "Time-resolved Measurements of the Optical Properties of Fibrous Media Using the Anisotropic Diffusion Equation," *Journal of Biomedical Optics* 19, no. 7 (2014): 075006, https://doi.org/10.1117/1.JBO.19.7.075006.

4. A. Nazarian, S. L. Jacques, J. Tam, R. R. Anderson, and S. J. Shefelbine, "Structure of Tendon Causes Highly Optical Anisotropic Properties and Transport," *Journal of Biomedical Optics* 31, no. 3 (2026): 035003, https://doi.org/10.1117/1.JBO.31.3.035003.

5. A. Kienle, F. K. Forster, R. Diebolder, and R. Hibst, "Light Propagation in Dentin: Influence of Microstructure on Anisotropy," *Physics in Medicine and Biology* 48, no. 2 (2002): N7, https://doi.org/10.1088/0031-155/48/2/401.

6. C. J. Zoller, A. Hohmann, F. Foschum, et al., "Parallelized Monte Carlo Software to Efficiently Simulate the Light Propagation in Arbitrarily Shaped Objects and Aligned Scattering Media," *Journal of Biomedical Optics* 23, no. 6 (2018): 065004, https://doi.org/10.1117/1.JBO.23.6.065004.

7. S. Nickell, M. Hermann, M. Essenpreis, et al., "Anisotropy of Light Propagation in Human Skin," *Physics in Medicine and Biology* 45, no. 10 (2000): 2873, https://doi.org/10.1088/0031-155/45/10/310.

8. A. Sviridov, V. Chernomordik, M. Hassan, et al., "Intensity Profiles of Linearly Polarized Light Backscattered from Skin and Tissue-like Phantoms," *Journal of Biomedical Optics* 10, no. 1 (2005): 014012, https://doi.org/10.1117/1.1854677.

9. A. Kienle, C. D'Andrea, F. Foschum, P. Taroni, and A. Pifferi, "Light Propagation in Dry and Wet Softwood," *Optics Express* 16, no. 13 (2008): 9895, https://doi.org/10.1364/OE.16.009895.

10. R. Shanker, M. Hoglund, H. Chen, L. A. Berglund, and I. Sychugov, "Spatiotemporally Resolved Light Propagation in Transparent Wood," *Advanced Optical Materials* 13, no. 32 (2025): e01789, https://doi.org/10.1002/adom.202501789.

11. E. Pini, P. Naglič, M. Bürmen, et al., "Experimental Determination of Effective Light Transport Properties in Fully Anisotropic Media," *Advanced Photonics Nexus* 3, no. 5 (2024): 056017, https://doi.org/10.1117/1.APN.3.5.056017.

12. P. M. Johnson and A. Lagendijk, "Optical Anisotropic Diffusion: New Model Systems and Theoretical Modeling," *Journal of Biomedical Optics* 14, no. 5 (2009): 054036, https://doi.org/10.1117/1.3253332.

13. E. Pini, F. Martelli, A. Gatto, H. Schäfer, D. S. Wiersma, and L. Pattelli, "Diffusion of Light in Structurally Anisotropic Media with Uniaxial Symmetry," *Physical Review Research* 6, no. 2 (2024): 023051, https://doi.org/10.1103/PhysRevResearch.6.023051.

14. A. Kienle, C. Wetzel, A. Bassi, et al., "Determination of the Optical Properties of Anisotropic Biological Media Using an Isotropic Diffusion Model," *Journal of Biomedical Optics* 12, no. 1 (2007): 014026, https://doi.org/10.1117/1.2709864.

15. L. Cortese, L. Pattelli, F. Utel, et al., "Anisotropic Light Transport in White Beetle Scales," *Advanced Optical Materials* 3, no. 10 (2015): 1337, https://doi.org/10.1002/adom.201500173.

16. X. Chen and O. Korotkova, "Optical Beam Propagation in Soft Anisotropic Biological Tissues," *OSA Continuum* 1, no. 3 (2018): 1055, https://doi.org/10.1364/OSAC.1.001055.

17. G. Jacucci, O. D. Onelli, A. De Luca, et al., "Coherent Backscattering of Light by an Anisotropic Biological Network," *Interface Focus* 9, no. 1 (2019): 20180050, https://doi.org/10.1098/rsfs.2018.0050.

18. M. Soltaninezhad, A. Bavali, Z. Nazifinia, and V. Soleimani, "Optical Anisotropy Measurement in Normal and Cancerous Tissues: Backscattering Technique," *Biomedical Optics Express* 11, no. 6 (2020): 2996, https://doi.org/10.1364/BOE.393079.

19. S. E. Han, "Transport Mean Free Path Tensor and Anisotropy Tensor in Anisotropic Diffusion Equation for Optical Media," *Journal of Optics* 22, no. 7 (2020): 075606, https://doi.org/10.1088/2040-986/ab954d.

20. P. Li, C. Liu, X. Li, H. He, and H. Ma, "GPU Acceleration of Monte Carlo Simulations for Polarized Photon Scattering in Anisotropic Turbid Media," *Applied Optics* 55, no. 27 (2016): 7468, https://doi.org/10.1364/AO.55.007468.

21. X. Liu, X. Chen, C. Zhao, and B. Wang, "Polarized Light Transport in Anisotropic Media Composed of Ellipsoids: Influence of Structural Anisotropy," *Journal of Quantitative Spectroscopy and Radiative Transfer* 245 (2020): 106854, https://doi.org/10.1016/j.jqsrt.2020.106854.

22. X. Liu, B. Wang, J. Chen, and C. Zhao, "Polarization Signatures of Structural Anisotropy for Radiative Transfer in Fibrous Materials," *Journal of Quantitative Spectroscopy and Radiative Transfer* 276 (2021): 107928, https://doi.org/10.1016/j.jqsrt.2021.107928.

23. T. Yun, N. Zeng, W. Li, et al., "Monte Carlo Simulation of Polarized Photon Scattering in Anisotropic Media," *Optics Express* 17, no. 19 (2009): 16590, https://doi.org/10.1364/OE.17.016590.

24. A. Kienle, F. Foschum, and A. Hohmann, "Light Propagation in Structural Anisotropic Media in the Steady-State and Time Domains," *Physics in Medicine and Biology* 58, no. 17 (2013): 6205, https://doi.org/10.1088/0031-9155/58/17/6205.

25. R. Vasques and E. W. Larsen, "Non-Classical Particle Transport with Angular-Dependent Path-Length Distributions. I: Theory," *Annals of Nuclear Energy* 70 (2014): 292, https://doi.org/10.1016/j.anucene.2013.12.020.

26. F. Martelli, T. Binzoni, S. Del Bianco, A. Liemert, and A. Kienle, *Light Propagation Through Biological Tissue and Other Diffusive Media: Theory, Solutions, and Validations* (SPIE, 2022), https://doi.org/10.1117/3.2624517.

27. E. Alerstam, "Anisotropic Diffusive Transport: Connecting Microscopic Scattering and Macroscopic Transport Properties," *Physical Review E* 89, no. 6 (2014): 063202, https://doi.org/10.1103/PhysRevE.89.063202.

28. P. Naglič, Y. Zelinskyi, F. Pernuš, B. Likar, and M. Bürmen, "PyXOpto: An Open-Source Python Library with Utilities for Fast Light Propagation Modeling in Turbid Media," in European Conference on Biomedical Optics, *EM3C–2* (Optica Publishing Group, 2021), https://doi.org/10.1364/ECBO.2021.EM3C.2.

29. R. C. Haskell, L. O. Svaasand, T.-T. Tsay, et al., "Boundary Conditions for the Diffusion Equation in Radiative Transfer," *Journal of the Optical Society of America A* 11, no. 10 (1994): 2727, https://doi.org/10.1364/JOSAA.11.002727.

30. N. Nouri and A. Martin, "Three Dimensional Radiative Heat Transfer Model for the Evaluation of the Anisotropic Effective Conductivity of Fibrous Materials," *International Journal of Heat and Mass Transfer* 83 (2015): 629, https://doi.org/10.1016/j.ijheatmasstransfer.2014.12.041.

31. D. Wang, H. Ban, and P. Jiang, "Three-Dimensional (3D) Tensor-Based Methodology for Characterizing 3D Anisotropic Thermal Conductivity Tensor," *International Journal of Heat and Mass Transfer* 242 (2025): 126886, https://doi.org/10.1016/j.ijheatmasstransfer.2025.126886.

Appendix A: Diffusion Tensor Components for A Scalar Asymmetry Factor

For the case of anisotropic diffusion with $g \neq 0$, the diffusion tensor components can be written as [26]

$$D_{ij} = \frac{v}{4\pi\langle\ell\rangle}\int_{4\pi}\left(\frac{s_i}{\mu_s^2(\hat{\mathbf{s}})} - \frac{\zeta^i(\hat{\mathbf{s}})}{\mu_s(\hat{\mathbf{s}})}\right)s_j\,\mathrm{d}\Omega, \tag{A.1}$$

where

$$\zeta^i(\hat{\mathbf{s}}) = \sum_{n=0}^{\infty}\zeta_n^i(\hat{\mathbf{s}}), \tag{A.2}$$

with

$$\zeta_0^i(\hat{\mathbf{s}}) = \mathcal{S}^i(\hat{\mathbf{s}}) = -\int_{4\pi}\mathrm{d}\Omega' s_i' \frac{p(\hat{\mathbf{s}}\cdot\hat{\mathbf{s}}')}{\mu_s(\hat{\mathbf{s}}')}, \tag{A.3}$$

and

$$\zeta^i_{n+1}(\hat{\mathbf{s}}) = \int_{4\pi} \mathrm{d}\Omega' p(\hat{\mathbf{s}} \cdot \hat{\mathbf{s}}')\zeta^i_n(\hat{\mathbf{s}}'). \tag{A.4}$$

The Henyey–Greenstein phase function $p(\hat{\mathbf{s}} \cdot \hat{\mathbf{s}}')$ can be written in terms of spherical harmonics as

$$p(\hat{\mathbf{s}} \cdot \hat{\mathbf{s}}') = \sum_{l=0}^{\infty} \frac{(2l+1)}{4\pi} g^l P_l(\hat{\mathbf{s}} \cdot \hat{\mathbf{s}}') = \sum_{l=0}^{\infty} \sum_{m=-l}^{l} g^l Y_l^{m*}(\hat{\mathbf{s}}) Y_l^m(\hat{\mathbf{s}}'), \tag{A.5}$$

where the addition theorem of spherical harmonics has been used,

$$\frac{(2l+1)}{4\pi} P_l(\hat{\mathbf{s}} \cdot \hat{\mathbf{s}}') = \sum_{m=-l}^{l} Y_l^{m*}(\hat{\mathbf{s}}) Y_l^m(\hat{\mathbf{s}}'). \tag{A.6}$$

By substituting Equation (A.5) in Equation (A.3) one finds

$$\zeta^i_0(\hat{\mathbf{s}}) = \mathcal{S}^i(\hat{\mathbf{s}}) = -\sum_{l=0}^{\infty} \sum_{m=-l}^{l} g^l Y_l^{m*}(\hat{\mathbf{s}}) \int_{4\pi} \mathrm{d}\Omega' \frac{Y_l^m(\hat{\mathbf{s}}') s_i'}{\mu_\mathrm{s}(\hat{\mathbf{s}}')}, \tag{A.7}$$

which can be rewritten as

$$\zeta^i_0(\hat{\mathbf{s}}) = \mathcal{S}^i(\hat{\mathbf{s}}) = -\sum_{l=0}^{\infty} \sum_{m=-l}^{l} g^l Y_l^{m*}(\hat{\mathbf{s}}) H^i_{lm}, \tag{A.8}$$

with

$$H^i_{lm} = \int_{4\pi} \mathrm{d}\Omega' \frac{Y_l^m(\hat{\mathbf{s}}') s_i'}{\mu_\mathrm{s}(\hat{\mathbf{s}}')}, \tag{A.9}$$

which is a function of $\mu_{\mathrm{s},x}$, $\mu_{\mathrm{s},y}$ and $\mu_{\mathrm{s},z}$. Equation (A.8) is then replaced in Equation (A.4) with $n = 1$ to obtain

$$\begin{aligned} \zeta^i_1(\hat{\mathbf{s}}) &= \sum_{l=0}^{\infty} \sum_{m=-l}^{l} g^l Y_l^{m*}(\hat{\mathbf{s}}) \int_{4\pi} \mathrm{d}\Omega' \zeta^i_0(\hat{\mathbf{s}}') Y_l^m(\hat{\mathbf{s}}') \\ &= -\sum_{l=0}^{\infty} \sum_{m=-l}^{l} \sum_{l'=0}^{\infty} \sum_{m'=-l'}^{l'} g^{l+l'} Y_l^{m*}(\hat{\mathbf{s}}) H^i_{lm} \int_{4\pi} \mathrm{d}\Omega' Y_{l'}^{m'*}(\hat{\mathbf{s}}') Y_l^m(\hat{\mathbf{s}}') \\ &= -\sum_{l=0}^{\infty} \sum_{m=-l}^{l} g^{2l} Y_l^{m*}(\hat{\mathbf{s}}) H^i_{lm} \end{aligned} \tag{A.10}$$

where the orthonormality relation for the spherical harmonics has been used

$$\int_{4\pi} \mathrm{d}\Omega Y_l^{m*}(\hat{\mathbf{s}}) Y_{l'}^{m'}(\hat{\mathbf{s}}) = \delta_{l,l'} \delta_{m,m'}. \tag{A.11}$$

Similarly, it can be demonstrated by induction that

$$\zeta^i_n(\hat{\mathbf{s}}) = -\sum_{l=0}^{\infty} \sum_{m=-l}^{l} g^{(n+1)l} Y_l^{m*}(\hat{\mathbf{s}}) H^i_{lm}. \tag{A.12}$$

Substituting this result into Equation (A.2) returns

$$\zeta^i(\hat{\mathbf{s}}) = \sum_{n=0}^{\infty} \zeta^i_n(\hat{\mathbf{s}}) = -\sum_{l=0}^{\infty} \sum_{m=-l}^{l} Y_l^{m*}(\hat{\mathbf{s}}) H^i_{lm} g^l \sum_{n=0}^{\infty} g^{nl}, \tag{A.13}$$

which can be expressed as

$$\zeta^i(\hat{\mathbf{s}}) = -\sum_{l=0}^{\infty} \sum_{m=-l}^{l} \frac{g^l}{1-g^l} Y_l^{m*}(\hat{\mathbf{s}}) H^i_{lm}. \tag{A.14}$$

Inserting Equation (A.14) in Equation (A.1) yields

$$\begin{aligned} D_{ij} &= \delta_{ij} D_{ii}\Big|_{g=0} - \frac{\upsilon}{4\pi\langle\ell\rangle} \int_{4\pi} \frac{\zeta^i(\hat{\mathbf{s}}) s_j}{\mu_\mathrm{s}(\hat{\mathbf{s}})} \mathrm{d}\Omega \\ &= \delta_{ij} D_{ii}\Big|_{g=0} + \frac{\upsilon}{4\pi\langle\ell\rangle} \sum_{l=0}^{\infty} \sum_{m=-l}^{l} \frac{g^l}{1-g^l} H^i_{lm} \int_{4\pi} \mathrm{d}\Omega \frac{s_j Y_l^{m*}(\hat{\mathbf{s}})}{\mu_\mathrm{s}(\hat{\mathbf{s}})} \\ &= \delta_{ij} D_{ii}\Big|_{g=0} + \frac{\upsilon}{4\pi\langle\ell\rangle} \sum_{l=0}^{\infty} \sum_{m=-l}^{l} \frac{g^l}{1-g^l} H^i_{lm} H^{j,*}_{lm}. \end{aligned} \tag{A.15}$$

The expressions can now be simplified by exploiting the symmetries of spherical harmonics and of $\mu_\mathrm{s}(\hat{\mathbf{s}})$. If inversion of all coordinates $\hat{\mathbf{s}} \to -\hat{\mathbf{s}}$ is considered,

$$Y_l^m(-\hat{\mathbf{s}}) = (-1)^l Y_l^m(\hat{\mathbf{s}}), \quad \mu_\mathrm{s}(-\hat{\mathbf{s}}) = \mu_\mathrm{s}(\hat{\mathbf{s}}), \tag{A.16}$$

and therefore

$$H^i_{lm} = \int_{4\pi} \mathrm{d}\Omega \frac{Y_l^m(\hat{\mathbf{s}}) s_i}{\mu_\mathrm{s}(\hat{\mathbf{s}})} = \int_{4\pi} \mathrm{d}\Omega \frac{Y_l^m(-\hat{\mathbf{s}})(-s_i)}{\mu_\mathrm{s}(-\hat{\mathbf{s}})} = -(-1)^l H^i_{lm}, \tag{A.17}$$

which implies

$$H^i_{2l,m} = 0 \quad \forall l. \tag{A.18}$$

When instead the transformation $(x, y, z) \to (-x, -y, z)$, corresponding to $\phi \to \phi + \pi$, is considered,

$$Y_l^m(\theta, \phi + \pi) = (-1)^m Y_l^m(\theta, \phi), \quad \mu_\mathrm{s}(\theta, \phi + \pi) = \mu_\mathrm{s}(\theta, \phi), \tag{A.19}$$

and for the x and y components of H_{lm} one obtains

$$\begin{aligned} H^{x,y}_{lm} &= \int_{4\pi} \mathrm{d}\Omega \frac{Y_l^m(\theta, \phi) s_{x,y}(\theta, \phi)}{\mu_\mathrm{s}(\theta, \phi)} \\ &= \int_{4\pi} \mathrm{d}\Omega \frac{Y_l^m(\theta, \phi + \pi) s_{x,y}(\theta, \phi + \pi)}{\mu_\mathrm{s}(\theta, \phi + \pi)} = -(-1)^m H^{x,y}_{lm}, \end{aligned} \tag{A.20}$$

and similarly for the z component

$$H^z_{lm} = (-1)^m H^z_{lm}, \tag{A.21}$$

from which it follows that

$$H^z_{2l,2m+1} = H^{x,y}_{2l,2m} = 0 \quad \forall l, m. \tag{A.22}$$

If a reflection about the y axis is considered, mapping $\phi \to -\phi$, one has

$$Y_l^m(\theta, -\phi) = Y_l^{m*}(\theta, \phi), \quad \mu_\mathrm{s}(\theta, -\phi) = \mu_\mathrm{s}(\theta, \phi), \tag{A.23}$$

which gives

$$H^{x,z}_{lm} = H^{x,z*}_{lm}, \quad H^y_{lm} = -H^{y*}_{lm} \quad \forall l, m, \tag{A.24}$$

that is, the x and z components of H_{lm} are real, while the y component is imaginary.

Furthermore, since $Y_l^{-m}(\theta, \phi) = (-1)^m Y_l^{m*}(\theta, \phi)$, from Equation (A.9) one can also find

$$H^i_{l,-m} = (-1)^m H^{i*}_{l,m} \quad \forall l, m. \tag{A.25}$$

It can now be demonstrated that the contributions to the off-diagonal elements of the diffusion tensor D_{ij} vanish for $g \neq 0$. By using Equation (A.22), it follows that

$$H^{x,y}_{2l,m} H^{z*}_{2l,m} = 0 \quad \forall m, \tag{A.26}$$

because for each m one of the two factors is identically zero. As for the tensor components D_{xy} and D_{yx}, by using Equations (A.18), (A.22), (A.24), (A.25) the sum over m in Equation (A.15) can be rewritten as

$$\begin{aligned}\sum_{m=-2l-1}^{2l+1} H^x_{2l+1,m} H^{y*}_{2l+1,m} &= \sum_{m=0}^{l} \left(H^x_{2l+1,2m+1}H^{y*}_{2l+1,2m+1} + H^x_{2l+1,-2m-1}H^{y*}_{2l+1,-2m-1}\right)\\ &= \sum_{m=0}^{l} \left(H^x_{2l+1,2m+1}H^{y*}_{2l+1,2m+1} + H^{x*}_{2l+1,2m+1}H^{y}_{2l+1,2m+1}\right)\\ &= \sum_{m=0}^{l} 2\mathrm{Re}\left(H^x_{2l+1,2m+1}H^{y*}_{2l+1,2m+1}\right) = 0.\end{aligned} \tag{A.27}$$

Finally, this allows us to write the diffusion tensor components as

$$D_{ij} = \delta_{ij} D_{ii}\Big|_{g=0} + \frac{v\delta_{ij}}{4\pi\langle\ell\rangle} \sum_{n=0}^{\infty} \sum_{m=-2n-1}^{2n+1} \frac{g^{2n+1}}{1-g^{2n+1}} \left|H^i_{2n+1,m}\right|^2. \tag{A.28}$$

Using the symmetry $\left|H^i_{l,-m}\right|^2 = \left|H^i_{l,m}\right|^2$ together with the selection rules derived above, only a subset of the m indices contributes to the sum. In particular, for odd angular orders $l = 2n+1$, the non-vanishing terms can be grouped pairwise, allowing the expression for the diagonal diffusion tensor elements to be written in the more compact form used in the main text

$$D_i = D_i\Big|_{g=0} + \frac{v}{4\pi\langle\ell\rangle} \sum_{n=0}^{\infty} \frac{g^{2n+1}}{1-g^{2n+1}} \sum_{m=-n}^{n} \left|H^i_{2n+1,2m}\right|^2. \tag{A.29}$$

In the isotropic limit, Equation (A.29) reduces to the expected form $\lim_{\mu_s(\hat{\mathbf{s}})\to\mu_s} D_i = v/(3\mu_s) + vg/[3\mu_s(1-g)] = v/[3\mu_s(1-g)]$.

Appendix B: Direction-Dependent Persistence Length

In the presence of a scalar single-scattering asymmetry factor g, directional correlations persist over multiple scattering events and modify the effective length scale entering boundary conditions and source-depth placement. A direction-dependent *persistence length* $\lambda(\hat{\mathbf{s}})$ is introduced here, which provides the exact length scale for a Henyey–Greenstein phase function with scalar g.

Let $\hat{\mathbf{s}}_0, \hat{\mathbf{s}}_1, \ldots$ denote successive propagation directions of a random walker undergoing scattering with phase function $p(\hat{\mathbf{s}}\cdot\hat{\mathbf{s}}')$. The conditional persistence vector is defined as

$$\boldsymbol{\Lambda}(\hat{\mathbf{s}}) = \left\langle \sum_{n=0}^{\infty} \ell(\hat{\mathbf{s}}_n)\hat{\mathbf{s}}_n \middle| \hat{\mathbf{s}}_0 = \hat{\mathbf{s}} \right\rangle, \tag{B.1}$$

where $\ell(\hat{\mathbf{s}}) = 1/\mu_s(\hat{\mathbf{s}})$ is the direction-dependent mean free path.

This quantity satisfies the renewal equation

$$\boldsymbol{\Lambda}(\hat{\mathbf{s}}) = \ell(\hat{\mathbf{s}})\hat{\mathbf{s}} + \int_{4\pi} p(\hat{\mathbf{s}}\cdot\hat{\mathbf{s}}')\boldsymbol{\Lambda}(\hat{\mathbf{s}}')\mathrm{d}\Omega'. \tag{B.2}$$

Introducing the scattering operator

$$(Kf)(\hat{\mathbf{s}}) = \int_{4\pi} p(\hat{\mathbf{s}}\cdot\hat{\mathbf{s}}') f(\hat{\mathbf{s}}')\mathrm{d}\Omega', \tag{B.3}$$

Equation (B.2) can be written as $(\mathbb{I} - K)\boldsymbol{\Lambda} = \ell(\hat{\mathbf{s}})\hat{\mathbf{s}}$.

The scalar persistence length relevant for boundary conditions is obtained by projecting $\boldsymbol{\Lambda}$ along the initial propagation direction,

$$\lambda(\hat{\mathbf{s}}) = \hat{\mathbf{s}}\cdot\boldsymbol{\Lambda}(\hat{\mathbf{s}}) = \left\langle \sum_{n=0}^{\infty} \ell(\hat{\mathbf{s}}_n)(\hat{\mathbf{s}}_n\cdot\hat{\mathbf{s}}) \middle| \hat{\mathbf{s}}_0 = \hat{\mathbf{s}} \right\rangle. \tag{B.4}$$

For a scalar Henyey–Greenstein phase function, the scattering operator is diagonal in spherical harmonics (Equation (A.5)). As a consequence, the resolvent $(\mathbb{I} - K)^{-1}$ introduces factors $(1-g^l)^{-1}$ in each angular momentum channel.

Since $\ell(\hat{\mathbf{s}})\hat{\mathbf{s}}$ is odd under inversion $\hat{\mathbf{s}} \to -\hat{\mathbf{s}}$, only odd Legendre orders contribute to the solution. Using the spherical-harmonic addition theorem, the persistence length can be written directly in terms of Legendre polynomials as

$$\lambda(\hat{\mathbf{s}}) = \sum_{n=0}^{\infty} \frac{4n+3}{4\pi} \frac{1}{1-g^{2n+1}} \int_{4\pi} \frac{\hat{\mathbf{s}}\cdot\hat{\mathbf{s}}' P_{2n+1}(\hat{\mathbf{s}}\cdot\hat{\mathbf{s}}')}{\mu_s(\hat{\mathbf{s}}')}\mathrm{d}\Omega'. \tag{B.5}$$

Notably, Equation (B.5) reduces to the expected limits $\lim_{g\to 0}\lambda(\hat{\mathbf{s}}) = \ell(\hat{\mathbf{s}})$ and $\lim_{\mu_s(\hat{\mathbf{s}})\to\mu_s}\lambda(\hat{\mathbf{s}}) = \ell/(1-g) = \ell^*$.

Appendix C: Derivation of the Boundary-Condition Integral $\mathcal{Y}$ With Fresnel Reflections

In this appendix the boundary-condition integral $\mathcal{Y}$ entering the extrapolated length z_e is derived in the presence of Fresnel reflections at the slab boundaries. The derivation closely follows Appendix A; therefore, only the steps that differ from the bulk calculation are reported.

The boundary-condition integral $\mathcal{Y}$ is defined as

$$\mathcal{Y} = \frac{1}{4\pi\langle\ell\rangle} \int_{\Omega_{\mathrm{up}}} \left(\frac{s_z^2}{\mu_s^2(\hat{\mathbf{s}})} - \frac{s_z\zeta^z(\hat{\mathbf{s}})}{\mu_s(\hat{\mathbf{s}})} \right) R(\theta)\mathrm{d}\Omega, \tag{C.1}$$

where Ω_{up} denotes the upper hemisphere ($s_z > 0$) and $R(\theta)$ is the Fresnel reflection coefficient defined in Equation (32). The auxiliary function $\zeta^z(\hat{\mathbf{s}})$ is the z component of Equation (A.14), since its defining integral equation involves only bulk scattering properties and is unaffected by boundary reflections.

Substituting the expression for $\zeta^z(\hat{\mathbf{s}})$ into Equation (C.1) yields

$$\begin{aligned}\mathcal{Y} = &\frac{1}{4\pi\langle\ell\rangle} \int_{\Omega_{\mathrm{up}}} \frac{s_z^2}{\mu_s^2(\hat{\mathbf{s}})} R(\theta)\mathrm{d}\Omega\\ &+ \frac{1}{4\pi\langle\ell\rangle} \sum_{l=0}^{\infty}\sum_{m=-l}^{l} \frac{g^l}{1-g^l} H^z_{lm} \int_{\Omega_{\mathrm{up}}} \frac{s_z}{\mu_s(\hat{\mathbf{s}})} Y_l^{m*}(\hat{\mathbf{s}}) R(\theta)\mathrm{d}\Omega.\end{aligned} \tag{C.2}$$

Because the angular integration is restricted to the upper hemisphere, the orthonormality relations of the spherical harmonics over 4π can no longer be exploited. It is therefore convenient to introduce the hemisphere-weighted projection coefficient

$$\widetilde{H}^z_{lm} = \int_{\Omega_{\mathrm{up}}} \frac{s_z}{\mu_s(\hat{\mathbf{s}})} Y_l^{m*}(\hat{\mathbf{s}}) R(\theta)\mathrm{d}\Omega. \tag{C.3}$$

Using this definition, Equation (C.2) can be rewritten as

$$\mathcal{Y} = \mathcal{Y}\Big|_{g=0} + \frac{1}{4\pi\langle\ell\rangle} \sum_{l=0}^{\infty}\sum_{m=-l}^{l} \frac{g^l}{1-g^l} H^z_{lm}\widetilde{H}^z_{lm}, \tag{C.4}$$

where the isotropic-scattering contribution $\mathcal{Y}\Big|_{g=0}$ is given by Equation (37).

In full analogy with the selection rules derived in Appendix A, the sum is restricted to odd angular orders $l = 2n + 1$. The final expression for $\mathcal{Y}$ therefore becomes

$$\mathcal{Y} = \mathcal{Y}\Big|_{g=0} + \frac{1}{4\pi\langle \ell \rangle} \sum_{n=0}^{\infty} \frac{g^{2n+1}}{1 - g^{2n+1}} \sum_{m=-n}^{n} H^{z}_{2n+1,m} \widetilde{H}^{z}_{2n+1,m}. \tag{C.5}$$

In the isotropic limit, z_e tends to the standard form reported in Ref. [26], as expected.